

Structural basis for loading and inhibition of a bacterial T6SS phospholipase effector by the VgrG spike

Nicolas Flaugnatti^{1,†,‡}, Chiara Rapisarda^{2,3,†,§} , Martial Rey⁴, Solène G Beauvois¹, Viet Anh Nguyen¹, Stéphane Canaan¹ , Eric Durand¹ , Julia Chamot-Rooke⁴, Eric Cascales¹ , Rémi Fronzes^{2,3,*}  & Laure Journet^{1,**} 

Abstract

The bacterial type VI secretion system (T6SS) is a macromolecular machine that injects effectors into prokaryotic and eukaryotic cells. The mode of action of the T6SS is similar to contractile phages: the contraction of a sheath structure pushes a tube topped by a spike into target cells. Effectors are loaded onto the spike or confined into the tube. In enteroaggregative *Escherichia coli*, the Tle1 phospholipase binds the C-terminal extension of the VgrG trimeric spike. Here, we purify the VgrG–Tle1 complex and show that a VgrG trimer binds three Tle1 monomers and inhibits their activity. Using covalent cross-linking coupled to high-resolution mass spectrometry, we provide information on the sites of contact and further identify the requirement for a Tle1 N-terminal secretion sequence in complex formation. Finally, we report the 2.6-Å-resolution cryo-electron microscopy tri-dimensional structure of the (VgrG)₃–(Tle1)₃ complex revealing how the effector binds its cargo, and how VgrG inhibits Tle1 phospholipase activity. The inhibition of Tle1 phospholipase activity once bound to VgrG suggests that Tle1 dissociation from VgrG is required upon delivery.

Keywords bacterial competition; bacterial toxin; cryo-electron microscopy; protein secretion; type VI secretion system

Subject Categories Microbiology, Virology & Host Pathogen Interaction; Structural Biology

DOI 10.15252/embj.2019104129 | Received 27 November 2019 | Revised 24 March 2020 | Accepted 25 March 2020

The EMBO Journal (2020) e104129

Introduction

The type VI secretion system (T6SS) is a multiprotein secretion nano-machine used by many Gram-negative bacteria to deliver toxins in a contact-dependent manner directly into target cells. The T6SS can target both eukaryotic and prokaryotic cells, secreting effectors that degrade the peptidoglycan (amidases, glycoside hydrolases), membranes (phospholipases A₁, A₂ and D) or DNA (DNases) (Durand *et al*, 2014; Russell *et al*, 2014; Cianfanelli *et al*, 2016; Hachani *et al*, 2016). Some anti-host effectors interfere with eukaryotic cytoskeleton dynamics (actin, microtubules), leading to phagocytosis inhibition or promoting invasion (Durand *et al*, 2014; Russell *et al*, 2014; Cianfanelli *et al*, 2016; Hachani *et al*, 2016). The T6SS secretion of antibacterial effectors allows bacteria to eliminate competitors, to acquire nutrients, new DNA or metal, thus favouring the colonization of specific niches (Durand *et al*, 2014; Russell *et al*, 2014; Cianfanelli *et al*, 2016; Hachani *et al*, 2016).

T6SS biogenesis needs at least 14 different proteins. These subunits assemble two sub-complexes: a membrane complex anchored in the envelope (Durand *et al*, 2015; Rapisarda *et al*, 2019), on which a platform that controls the assembly of a contractile tail tube/sheath structure is docked (Basler *et al*, 2012; Brunet *et al*, 2015; Logger *et al*, 2016; Taylor *et al*, 2016; Nguyen *et al*, 2017; Nazarov *et al*, 2018). The tail tube/sheath complex comprises an inner tube made of Hcp hexamers covered by a sheath and topped by a needle spike constituted of a VgrG trimer and a PAAR-domain protein (Ho *et al*, 2014; Zoued *et al*, 2014). The tail sheath assembles in an extended conformation, and its contraction propels the inner tube, the spike and toxins towards target cells. Self-protection is assured by immunity proteins that specifically bind and inhibit their corresponding effectors. A few T6SS effectors are fused to the

1 Laboratoire d'Ingénierie des Systèmes Macromoléculaires, Institut de Microbiologie de la Méditerranée, Aix-Marseille Université—CNRS UMR7255, Marseille, France

2 Institut Européen de Chimie et Biologie, University of Bordeaux, Pessac, France

3 CNRS UMR 5234 Microbiologie Fondamentale et Pathogénicité, Bordeaux, France

4 Mass Spectrometry for Biology Unit, Institut Pasteur, CNRS USR 2000, CITECH, Paris, France

*Corresponding author. Tel: +33 5 40 00 30 08; E-mail: r.fronzes@iecb.u-bordeaux.fr

**Corresponding author. Tel: +33 4 91 16 44 62; E-mail: ljournet@imm.cnrs.fr

†These authors contributed equally to this work

‡Present address: Laboratory of Molecular Microbiology, Global Health Institute, School of Life Sciences, Ecole Polytechnique Fédérale de Lausanne (EPFL), Lausanne, Switzerland

§Present address: UCB Pharma, Slough, UK

Hcp, VgrG or PAAR proteins and are therefore delivered into the recipient cell as domains of syringe components (Pukatzki *et al*, 2006; Blondel *et al*, 2009; Suarez *et al*, 2010; Brooks *et al*, 2013; Dong *et al*, 2013; Shneider *et al*, 2013; Ma *et al*, 2017). However, most T6SS effectors are independent polypeptides. Upon T6SS assembly, these effectors are loaded within the lumen of the Hcp tube or bind the VgrG/PAAR spike and are then transported as cargo (Durand *et al*, 2014; Ho *et al*, 2014; Cianfanelli *et al*, 2016). Small effectors (< 20 kDa), such as the *Pseudomonas aeruginosa* Tse2 toxin, have been shown to fill the internal hole of Hcp hexamers (Silverman *et al*, 2013), whereas others have been demonstrated to indirectly interact with VgrG. Binding of these effectors is mediated by specific adaptors (Alcoforado Diniz & Coulthurst, 2015; Liang *et al*, 2015; Unterweger *et al*, 2015; Bondage *et al*, 2016). These adaptors are not secreted components but are rather required for the secretion of their cognate effectors, suggesting a role in loading effectors to VgrG prior to translocation. A complex constituted of the PAAR-fused Tse6 effector, the EagT6 adaptor, the immunity to Tse6 and EF-Tu was recently visualized by negative stain electron microscopy (EM). It forms a horseshoe-like structure at the tip of the VgrG trimer (Whitney *et al*, 2015). The cryo-EM structure of Tse6–EagT6 in complex with VgrG was further determined (Quentin *et al*, 2018).

We recently identified Tle1, a periplasmic-acting phospholipase A₁ (PLA1) antibacterial effector of the enteroaggregative *Escherichia coli* (EAEC) T6SS-1 (Flaunatti *et al*, 2016). We showed that Tle1 is transported into the periplasm of target cells using the VgrG spike protein as carrier. In contrast to other VgrG-dependent effectors, Tle1 interacts directly with VgrG, without the need for a PAAR or adaptor protein. VgrG from EAEC possesses a C-terminal extension that comprises a DUF2345 and a transthyretin-like domain (TTR) responsible for the interaction with Tle1 (Flaunatti *et al*, 2016). Here, we report the purification of the VgrG–Tle1 complex and show that three Tle1 effectors bind to the VgrG trimer. Our data reveal that VgrG inhibits Tle1 PLA1 activity, and hence that Tle1 needs to be dissociated from its carrier once in the target cell. Using a combined approach of cross-linking mass spectrometry, deletion studies and functional assays, we identify the motifs involved in VgrG–Tle1 interaction, confirming the importance of the VgrG TTR domain and highlighting an N-terminal interaction motif within Tle1. Finally, we present the cryo-EM structure of Tle1 bound to the VgrG needle.

Results

Purification of the VgrG–Tle1 complex reveals that three Tle1 effectors bind to the VgrG trimer

We previously showed that Tle1 from EAEC interacts directly with the C-terminal domain extension of the VgrG spike protein (Flaunatti *et al*, 2016). To gain further insight into the VgrG–Tle1 complex, affinity-tagged VgrG and Tle1 proteins were co-produced in *E. coli*. The position of the affinity tag on each protein was rationally chosen to maintain the VgrG–Tle1 interaction: a Strep-tagII was fused to the N-terminus of VgrG (^SVgrG) to maintain the C-terminal Tle1-interacting motif available, and a 6×His-tag was fused to the Tle1 C-terminus (Tle1^H), as previous bacterial two-hybrid (BACTH) analysis suggested

that T25/T18 fusion at the N-terminus of Tle1 protein impaired the interaction with VgrG (Flaunatti *et al*, 2016). A complex containing both ^SVgrG and Tle1^H was purified to homogeneity using a two-step affinity purification and gel filtration (Fig EV1A). When subjected to size-exclusion chromatography analyses, ^SVgrG separated with an apparent mass of ~ 500 kDa (Fig EV1B, black line; Appendix Fig S1), which is higher than the 280-kDa theoretical mass of a VgrG trimer. This could be due to an artefact of the gel filtration technique, to the elongated-shape structure of the VgrG β-helix (Leiman *et al*, 2009; Uchida *et al*, 2014; Spínola-Amilibia *et al*, 2016), or this species may correspond to a dimer of a VgrG trimer. Once bound to Tle1^H, we observed an increase in the apparent molecular mass (Fig EV1B, blue line). Native-purified Tle1 was previously shown to be monomeric in solution, with an apparent molecular mass of 66 kDa (Flaunatti *et al*, 2016). Taken together, these results suggest that several Tle1 proteins are bound to the VgrG trimer. To provide further information on the stoichiometry of the ^SVgrG–Tle1^H complex, we performed quantitative in-gel SYPRO Ruby staining. This analysis of the purified ^SVgrG–Tle1^H complex gave a 1:0.92 molar ratio (Fig EV1C). The approximate 1:1 stoichiometry suggests that three Tle1 effectors are bound to a VgrG trimer.

High-resolution cross-linking mass spectrometry (XL-MS) mapping identifies VgrG–Tle1 sites of contact

To provide detailed information on the VgrG–Tle1 interaction, the ^SVgrG–Tle1^H complex was subjected to cross-linking with the NNP9 cross-linker (Nury *et al*, 2015). NNP9 was specifically engineered to carry 2 NHS carbamate reactive groups, which are less prone to hydrolysis than widely used NHS esters, thus improving cross-linking efficiency and performance compared to the commercial ones (Nury *et al*, 2015). Mass spectrometry analysis of cross-linked peptides revealed that VgrG and Tle1 establish numerous contacts (Fig 1A, Dataset EV1). In agreement with previous findings demonstrating that Tle1 binds the VgrG C-terminal TTR extension as well as a second upstream motif (Flaunatti *et al*, 2016), XL-MS showed that Tle1 binds the VgrG TTR motif and a second motif located in the C-terminal part of the gp27-like domain (Fig 1A). Accordingly, Tle1^H no longer co-purified with a ^SVgrG variant lacking the C-terminal 616–841 residues (^SVgrG_{ΔCTD}) (Appendix Fig S2A and B). More importantly, several cross-links involving Lys residues in the VgrG TTR domain and at the Tle1 N-terminus (K29, K30) were detected (Fig 1A and Appendix Fig S3A), suggesting that the VgrG TTR binds the Tle1 N-terminus. Interestingly, a sequence alignment of Tle1 orthologs reveals a striking difference at their N-termini. Compared to specialized Tle1 orthologs that are fused to Hcp, PAAR and VgrG proteins, isolated Tle1 proteins bear an N-terminal 26-amino acid extension (NT) (Fig 1B and Appendix Fig S3B). As deletion of the Tle1 NT region (Tle1_{Δ1–26}) did not impact PLA1 specific activity (Appendix Fig S4), this region is not necessary for Tle1 folding and activity. Tle1 NT extension is followed by a Lys-rich linker that precedes the Tle1-domain region (Appendix Fig S3). Substitution of these lysines by glutamate residues (K28K29K30–E28E29E30) did not impair Tle1 antibacterial activity against *E. coli* K12 (Fig 1C), suggesting that the K29 and K30 residues identified by XL-MS are not directly involved in the interaction with VgrG. Rather, the XL-MS data highlight the proximity of the NT and the TTR region in

the complex and we hypothesized that the NT region might be an important determinant of a Tle1 secretion signal allowing VgrG recognition and binding. Evidence for the crucial role of this extension was provided by co-immunoprecipitation (Fig 1D) and co-purification (Appendix Fig S2C) assays, which demonstrated that deletion of the Tle1 N-terminal 26 amino acids strongly affects the interaction with VgrG. To further test the importance of this VgrG interaction motif for the delivery of Tle1, we tested the ability of Tle1 Δ_{1-26} to complement a *tle1* knockout mutant in antibacterial competition (Fig 1C). While the production levels of Tle1 and Tle1 Δ_{1-26} were comparable, only Tle1 restored the killing defect of the *tle1* knockout mutant. Taken together, these results showed that Tle1 binds two regions of VgrG including the C-terminal TTR extension, whereas the Tle1 N-terminal 26-amino acid region is required for VgrG binding and translocation into target cells.

Cryo-EM structure of the VgrG–Tle1 complex

Architecture of the VgrG spike–Tle1 complex

To gain further information on the structure of the VgrG–Tle1 complex, the purified 5 VgrG–Tle1^H complex was analysed using single-particle cryo-EM. The structure of the complex at 2.7 Å resolution overall was obtained by applying no symmetry (Fig EV2A and B). The 2D classes resembled violin bodies and were found in different orientations (Fig EV2A). From the unmasked cryo-EM density, we can observe the presence of a D3 symmetry with the dihedral rotational centre found between the two prism-like densities and further strengthened by opposite flexible densities interacting with each other (Fig EV2B and C). This large symmetric complex is 225 Å tall and 150 Å large and consists of 6 VgrG and 6 Tle1 densities as inferred from the gel

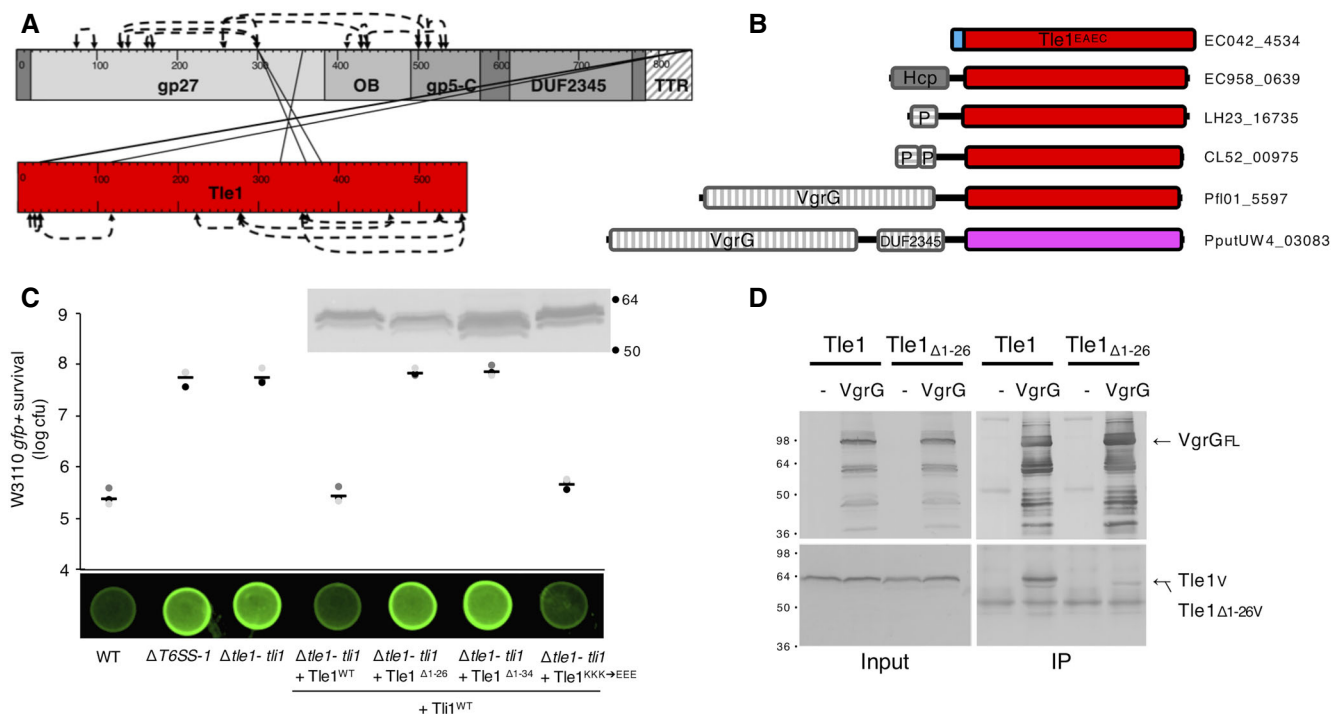


Figure 1. The N-terminal extension of Tle1 is required for VgrG-mediated transport into target cells.

- A Cross-link connectivity map of 5 VgrG–Tle1^H complex. The two proteins are represented as rectangles in which the residue number and known domains are indicated. Straight lines represent inter-molecular cross-links, while dotted lines represent intra-molecular cross-links. Only the cross-links identified in two independent experiments were considered. Raw and cured data are provided in Dataset EV1.
- B Schematic representation of an alignment of Tle1 orthologs using ClustalW and draw alignment tool in KEGG (Kanehisa et al, 2017). Red box, bit score ≥ 200 ; pink box, bit score ≥ 80 –200. Ordered locus names of the identified genes are indicated on the right. Domains are represented in grey boxes (Hcp, PF05638; PAAR (P), PF05488; VgrG, PF05954, COG3501; DUF2345, PF10106). The N-terminal segment found in EAEC Tle1 protein and absent in the others is represented by a blue box.
- C Antibacterial competition assay. *Escherichia coli* K12 recipient cells (W3110 *gfp*⁺, *kan*^R) were mixed with the indicated EAEC attacker cells (1:4 ratio): WT, Δ T6SS-1 and Δ tle1-*tlh1* carrying pBAD18 and pBAD33 vectors, or producing the indicated proteins, and spotted on SIM 0.02% arabinose agar plates for 4-h at 37°C. The image of the corresponding representative bacterial spots is presented and the number of recovered prey cells is indicated in the upper graph (in log of colony-forming units (cfu)). The black, dark grey and light grey circles indicate values obtained from three different spots, and the average is indicated by the bar. Western blot analysis of the production of Tle1_v and Tle1 Δ_{1-26} v is shown in the inset. The experiment was performed in triplicate, and a representative result is shown.
- D Co-immunoprecipitation assay. Lysates from *E. coli* K-12 W3110 cells producing VSVG-tagged Tle1 (Tle1_v) or VSVG-tagged Tle1 Δ_{1-26} truncated variant (Tle1 Δ_{1-26} v) were mixed with lysates from W3110 cells producing FLAG-tagged VgrG (VgrG_{FL}) or not (–, empty vector) and subjected to immunoprecipitation on anti-FLAG-coupled beads. The mixed soluble lysates (Input) and the immunoprecipitated material (IP) were subjected to 12.5% SDS–PAGE and immunodetected with anti-FLAG (upper panel) and anti-VSVG (lower panel) monoclonal antibodies. Molecular weight markers (in kDa) are indicated on the left. This experiment was performed in triplicate, and a representative result is shown.

Source data are available online for this figure.

filtration (Figs EV1B, and EV2B and C). This oligomeric state is likely not physiological. The absence of the PAAR capping protein may lead to this tip-to-tip VgrG needle spike interaction. We performed an unmasked refinement to 2.7 Å (Fig EV2B–D) followed by a local refinement on what we will hereby refer to as the physiological complex, consisting of 3 Tle1 and 3 VgrG molecules, and obtained a resolution of 2.6 Å (Figs 2A–C and EV2E). We further locally refined the prism-like density corresponding to VgrG (to 2.3 Å resolution), and one external density belonging to Tle1 (to 2.5 Å resolution) (Fig EV2F and G). Thanks to the high resolution of the cryo-EM densities obtained (Fig EV2E–G), we could build *de novo* an atomic model of VgrG amino acids (aa) 491–834 and of the full Tle1 (Figs 2D–H, and 3A and B), whose structures were previously unknown.

No interpretable cryo-EM density was found for VgrG amino acids 1–490. This region that is homologous to the gp27-like base followed by the gp5-OB fold-like in the T4 phage appears to be disordered. Such flexibility may be stabilized by binding of PAAR, and/or by the binding to baseplate components. This region is well conserved amongst the VgrG proteins from different bacterial species and phage families (Leiman *et al*, 2009). We therefore built a model using Phyre2 (Kelley *et al*, 2015), based on the sequence homology (42.5% identity) to the VgrG N-terminus from uropathogenic *E. coli* CFT073, whose structure has been solved by X-ray crystallography (Leiman *et al*, 2009; Fig 2G).

Structure of the gp5 needle-like domain of VgrG from EAEC

The atomic model of VgrG (aa 491–834) includes the gp5-C-like, DUF2345 and TTR domains predicted by bioinformatic analyses (Flaunatti *et al*, 2016; Figs 1A, and 2G and H). The region from aa 491 to 760 assembles a gp5 needle-like structure corresponding to a three-stranded β -prism with a width of 30 Å at the tip and 45 Å at the bottom (Fig 2G and H). The β -prism contains two anti-parallel β -sheets consisting of 5 and 3 strands respectively at aa 491–549 and 726–747 (Fig EV3A). Unique to the EAEC VgrG (VgrG^{EAEC}) is also the presence of two long helices that break the β -prism at aa 576–622. The rest of the β -prism is composed of parallel β -sheets that intertwine around each other via sharp β -turns (Fig EV3A). There is no cavity at the centre of the β -prism, and the structure is maintained by hydrophobic interactions (Fig 2H). The interaction between the monomers of VgrG, as calculated using PISA (Krissinel & Henrick, 2007), is very strong with a mean surface of interaction of 7,150 Å².

Comparison with the *P. aeruginosa* VgrG (VgrG^{PA}) structure and with the phage gp5 needle domain reveals several differences. In VgrG^{PA} (Fig EV3B, PDB: 4MTK), the gp5 needle domain is shorter by 40 Å because it only has a three-strand anti-parallel β -sheet at the base of the spike, instead of a 5-strand β -sheet (in blue, Fig EV3B). In the phage T4 gp5 protein (PDB: 1K28) (Kanamaru *et al*, 2002), there is only one anti-parallel 6-strand β -sheet at the base of the spike and none at the tip (in orange, Fig EV3C). VgrG^{EAEC} is unique also because it has an additional β -sheet TTR domain that binds the effector (Figs 2G and EV3D). This domain is missing in VgrG^{PA}, but it has been shown that the toxin does not directly bind to VgrG^{PA} but is covalently linked to the PAAR component (Whitney *et al*, 2015; Fig EV3E). In the T4 phage, gp5 has an additional lysozyme domain (Fig EV3F).

Structure of Tle1 bound to VgrG

The Tle1 structure bound to VgrG adopts a thin elongated shape, which is 125 Å tall and 50 Å wide on one side and 75 Å on the other (Fig 3A and B). It can be divided into three distinct domains: the finger N-terminal domain (aa 3–33), the phospholipase catalytic module (aa 33–326 and 411–539) and the lid domain (aa 327–410) (Figs 3A and EV4A). Two loops are missing from the density and are most likely disordered: aa 86–94 and aa 133–143. As shown by cross-linking MS, deletion analyses and co-purification (Fig 1D and Appendix Fig S2C), the finger domain is responsible for the interaction with the VgrG TTR domain and consists of a long loop that is highly flexible (Figs 3A–E, and EV4B and C). There is a smaller β -sheet composed of strand 17 at the C-terminus and strand 7 and an incomplete Greek key motif between strands 13–16 and 14–15 (Figs 3 and EV4A). The catalytic module has the most compact conformation and contains a classical α/β mixed hydrolase fold, composed of one central β -sheet of 6 β -strands (3-2-4-5-6-8) surrounded by α -helices (Figs 3A and B, and EV4A). The lid domain mainly comprises one long twisted anti-parallel β -sheet, constituted of three strands (11-12-9 and 10). In between strands 11 and 12, α -helix 12 (aa 338–395) mediates the interaction with the VgrG base (Figs 3A and B, and EV4A).

A new mechanism for T6SS effector loading on the VgrG spike

In contrast to the VgrG–chaperone–effector complex in *P. aeruginosa*, where the effector is fused to PAAR and located at the tip of the needle complex (Fig EV3E), the loading of Tle1 proteins on the VgrG spike is independent of PAAR. Moreover, three molecules of Tle1 are loaded on the VgrG trimer, on the sides of the β -prism (Fig 3F–H and Fig EV3D). Tle1 binds VgrG in three different regions (bottom, centre and top), and every VgrG chain interacts with each Tle1 monomer (Fig 3F–H and Table 1). The Tle1 catalytic domain interacts with the two α -helices (581–619) of one VgrG (chain A) and at the level of the β -prism with the two other VgrG monomers (chains B and C) (Fig 3F–H). The lid domain of Tle1 (aa 335–405) interacts only with chains B and C at the level of the anti-parallel β -sheet (Fig 3F–H). Finally, the finger domain of Tle1 (aa 3–33) and the loop of the catalytic domain (aa 225–230) between helix 8 and strand 5 interact with the TTR domain of VgrG (aa 778–841) (Fig 3C–E). The TTR domain is globular: it contains two sheets composed of 3 and 2 anti-parallel β -strands, respectively (Fig 3C–E). The finger domain of Tle1 complements the strands of the TTR domain to form a β -barrel (Fig 3C–E). The surface of interaction of VgrG with Tle1 is 1,160 Å² and has a ΔG of -12.2 kcal/M. The TTR–Tle1 interaction is mediated by several hydrogen bonds and salt bridges (Table 1). While VgrG is very stable, the finger domain and the TTR region are very flexible as shown by the B-factor values (Fig EV4B and C), and the local resolution (Appendix Fig S5) as the TTR domain is connected to the VgrG spike by a very flexible loop whose density was not resolved in the cryo-EM map.

Tle1 binding to VgrG inhibits its phospholipase activity

The Tle1 effector exhibits PLA1 activity *in vitro* (Flaunatti *et al*, 2016). In the cryo-EM structure of VgrG–Tle1, the catalytic module of Tle1 is well defined. It contains the phospholipase catalytic triad in an active conformation as the Ser197 and Asp245 residues are at a < 3 Å distance from His310 (Fig 3B). The catalytic triad is located

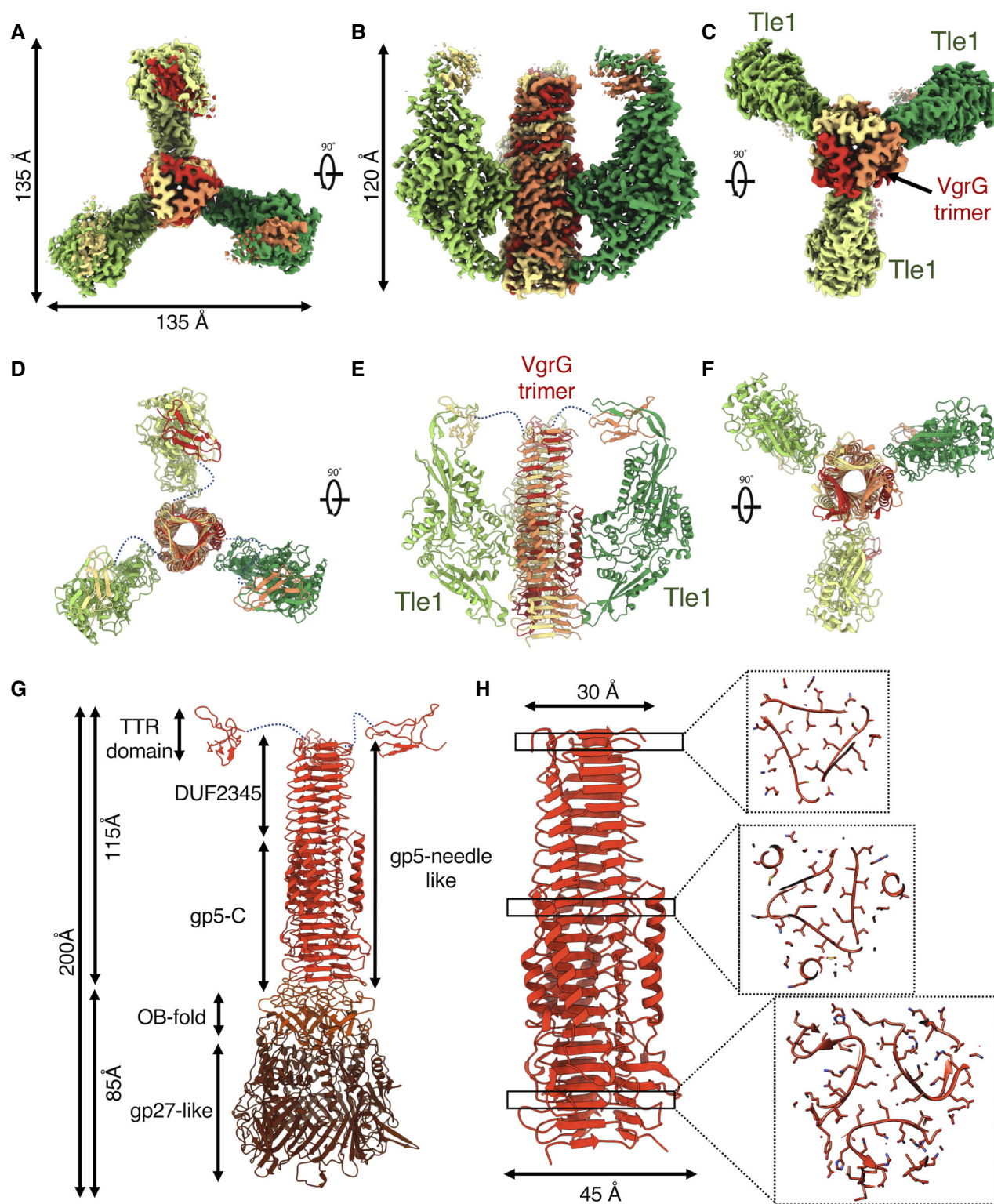


Figure 2. Cryo-EM density and pseudoatomic model of the VgrG needle (491–834) bound to Tle1.

A–C Autosharpened and masked cryo-EM density (Level 0.728) of the physiological complex in different orientations

D–F Ribbon diagram of the VgrG and Tle1 pseudoatomic structure, coloured according to the chain and in different orientations

G Full VgrG structure composed of the experimentally obtained spike (red) and the homology model of the base (dark red)

H Structure of the VgrG spike at different planes

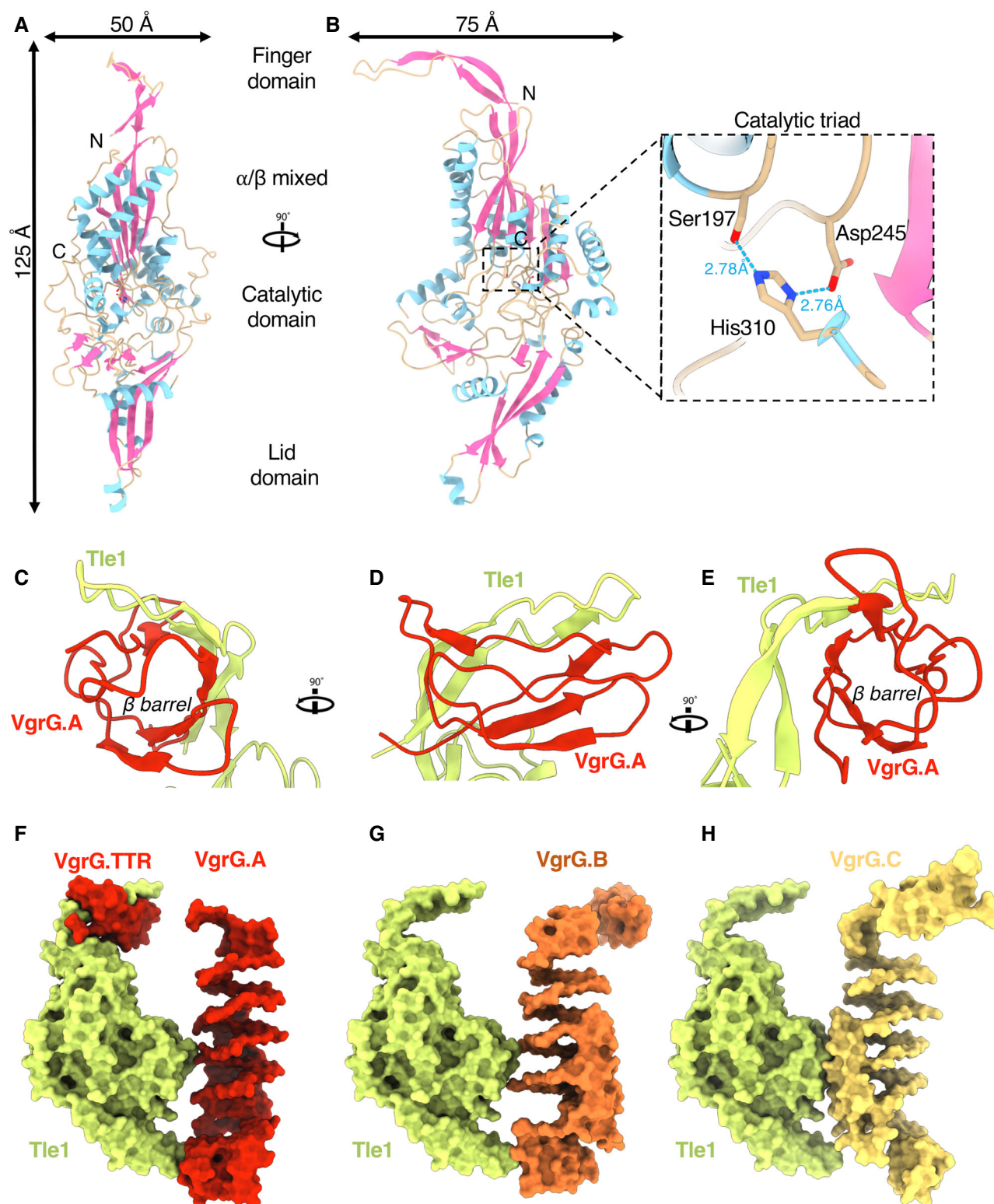


Figure 3. Tle1 structure and interaction with VgrG.

A, B Ribbon representation of the Tle1 pseudoatomic model. Strands are in pink and helices in light blue. The inset shows the catalytic triad.
C–E Ribbon representation of the interaction site between the Tle1 finger domain in yellow green and the VgrG TTR domain in red. The site is shown in different orientations.
F–H Molecular surface representation of the interactions between Tle1 chain D and chains A–C of VgrG, respectively (F–H).

Table 1. Interacting amino acids between VgrG and Tle1 as determined by PISA software.

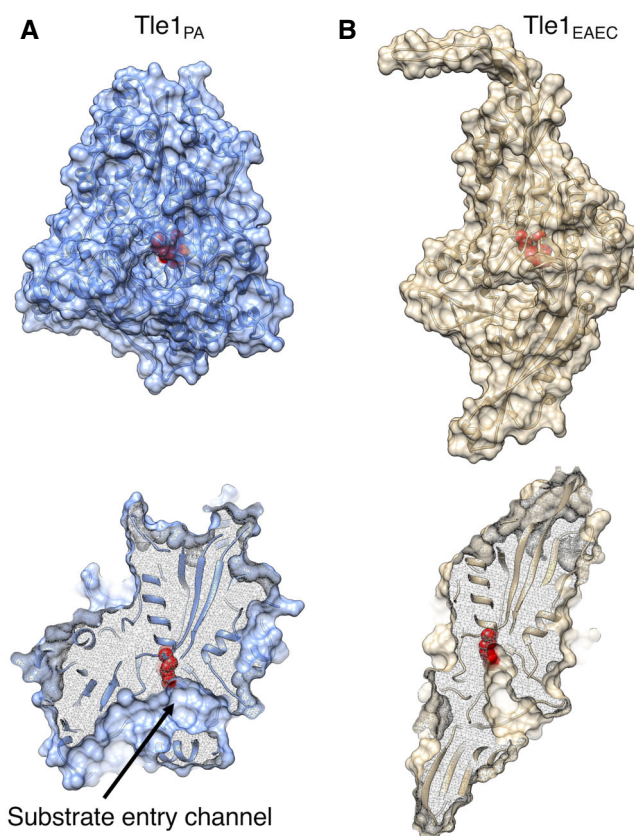
Interaction	H-bonds	Salt bridges
A–D	A.K596–D.F257	A.R592–D.E508
	A.K596–D.N260	
	A.Q612–D.D503	
	A.Q605–D.R513	
B–D		B.E513–D.R393
		B.D657–D.K517
C–D	C.G522–D.N390	
	C.E520–D.R393	
TTR–Tle1	G778–S17	D785–K29
	I782–V25	R797–D228
	I782–K23	
	T784–V25	
	S825–H14	
	V826–H14	
	K828–A12	

within a cavity that is positively charged at its end, with a hydrophobic entrance (Fig EV5A and B). However, comparison of the cryo-EM structure of Tle1^{EAEC} bound to VgrG to the *P. aeruginosa* Tle1 (Tle1^{PA}) crystal structure suggests that Tle1^{EAEC} PLA1 activity is inhibited by VgrG. In the Tle1^{PA} structure, a specific pocket allows binding of the phosphatidylglycerol moiety of the substrate at close proximity to the active site (Fig 4A; Hu *et al*, 2014). By contrast, in the Tle1^{EAEC} structure, this pocket is partially occluded by the lid domain. Remarkably, the position of the lid domain is constrained by the binding of its tip (helix 389–393) to VgrG (Fig 4B). In agreement with this observation, PLA1 activity of the purified ^SVgrG–Tle1^H complex was undetectable compared to the purified isolated Tle1^H protein (Fig 5A), suggesting that Tle1 binding to VgrG inhibits its activity. To confirm this VgrG-mediated inhibition, isolated Tle1^H purified protein was incubated with increasing amounts of purified ^SVgrG. Figure 5B shows that Tle1^H was inhibited by ^SVgrG in a dose-dependent manner, but not with the unrelated lysozyme protein. As a control, we purified ^SVgrG_{1–490}, a C-terminal truncated variant of VgrG deleted of the gp5 needle-like domain which mediates most of the contacts with Tle1^H (Fig 5C). In contrast to ^SVgrG, incubation of Tle1^H with ^SVgrG_{1–490} did not cause Tle1^H inhibition (Fig 5B).

Taken together, these results show that the Tle1 phospholipase activity is inhibited by VgrG in the ^SVgrG–Tle1^H complex, and hence that the Tle1 effectors have to be dissociated from VgrG to exhibit toxic PLA1 activity in the target cell.

Discussion

In this study, we provide a comprehensive picture of a complex between the T6SS VgrG spike protein and the phospholipase effector it recruits for translocation into target cells. We show that these two proteins form a complex with a 1:1 stoichiometry

**Figure 4.** Comparison of the active site of Tle1.

A, B Surface representation and cross section of Tle1 from *Pseudomonas aeruginosa* (PDB 4O5P) (A) and EAEC—this study (B). The active site is shown in red. The substrate entry channel is indicated when present.

comprising three Tle1 effectors bound to one VgrG trimer, suggesting that three Tle1 effectors are translocated into the target cell at each T6SS firing event. We further show that Tle1 recruitment to VgrG causes the inhibition of its activity. Bioinformatics, high-resolution mass spectrometry mapping and deletion studies combined with protein–protein interaction and functional assays demonstrated the importance of the N-terminal portion of Tle1 as a critical determinant for the interaction with the VgrG C-terminal TTR extension. Finally, we report the high-resolution cryo-EM structure of the Tle1 effector in complex with the needle/TTR portion of the VgrG spike. This structure confirms the importance of the TTR domain of VgrG for its interaction with the N-terminal finger domain of Tle1 and further highlights two previously unidentified regions of contact at the base and at the centre of the needle. Moreover, we provide a structural explanation for Tle1 inhibition by VgrG.

Structural model of the EAEC T6SS baseplate in a pre-firing state

VgrG is not only the spike of the needle but also the hub of the T6SS baseplate (BP) (Brunet *et al*, 2015; Taylor *et al*, 2016). The baseplate is the assembly platform for the tail tube/sheath complex and is docked to the TssJLM membrane complex (Brunet *et al*, 2015;

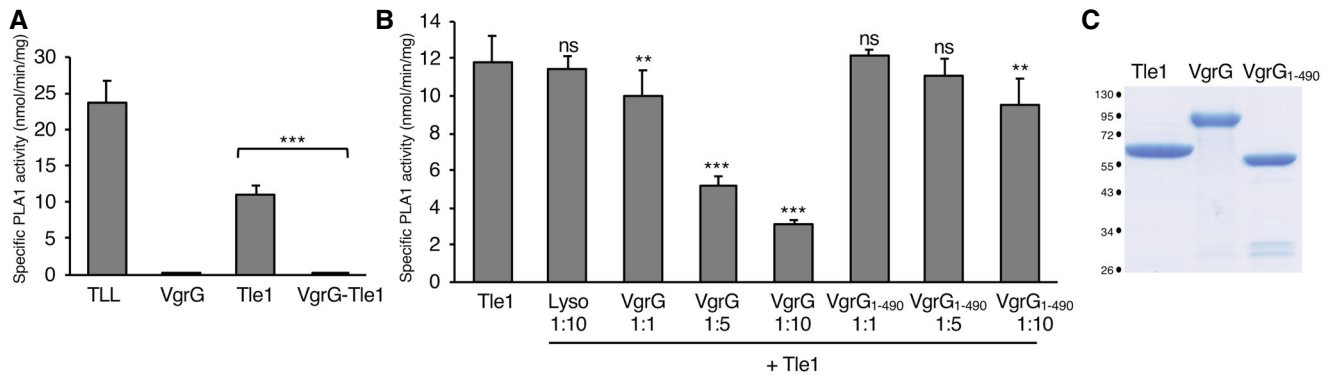


Figure 5. Inhibition of Tle1 by VgrG.

- A** Specific phospholipase A₁ (PLA₁) activity measurements of Tle1^H, ⁵VgrG–Tle1^H complex and isolated ⁵VgrG. *Thermomyces lanuginosus* lipase (TLL) was used as positive standard for PLA₁ activity. Mean values and standard deviation from at least three independent assays are shown. Statistical analysis relative to the Tle1 activity is indicated. ****P* < 0.001 (*P* = 0.0001998), unpaired two-sample Fisher–Pitman permutation test.
- B** VgrG inhibition of Tle1^H. Specific phospholipase A₁ (PLA₁) activity measurements of purified Tle1^H in the presence of 1:10 molar ratio of lysozyme from chicken egg white (Lyso) and increasing molar ratio (0, 1, 5 and 10) of ⁵VgrG or ⁵VgrG₁₋₄₉₀. Inhibition experiments with ⁵VgrG were repeated three times with independent protein preparations, each measured in triplicate. Mean values and standard deviation are shown. Statistical analysis relative to the Tle1 activity is indicated. ns, non-significant (*P* > 0.05), **P* < 0.05, ***P* < 0.01, ****P* < 0.001, unpaired two-sample Fisher–Pitman permutation test (*P*-values: Lyso, 0.7006; VgrG 1:1, 0.004946; VgrG 1:5, 1.448e-07; VgrG 1:10, 1.448e-07; VgrG₁₋₄₉₀ 1:1, 0.5627; VgrG₁₋₄₉₀ 1:5, 0.2977; VgrG₁₋₄₉₀ 1:10, 0.002631).
- C** Representative SDS–PAGE/Coomassie blue staining of the Tle1^H, ⁵VgrG and ⁵VgrG₁₋₄₉₀ purified proteins used in B (5 μg/well).

Source data are available online for this figure.

Zoued *et al*, 2016). The structure of the TssKFGE wedge complex of the baseplate was recently determined by cryo-EM (Cherrak *et al*, 2018). The structure of the fully assembled baseplate, including the VgrG hub surrounded by six wedges, was presented, based on the high-resolution wedge structure (Cherrak *et al*, 2018) and the baseplate lower resolution structure (Nazarov *et al*, 2018). We propose here a structural model of the EAEC T6SS baseplate including VgrG–Tle1 (Appendix Fig S6). Interestingly, the baseplate can readily accommodate the three Tle1 effectors (Appendix Fig S6). We propose that the VgrG–Tle1 structure represents the “pre-firing complex”.

A new mode of T6SS substrate loading

The VgrG–Tle1 complex represents the first example of direct binding of an effector on VgrG, which in general requires the PAAR subunit or an adaptor protein (Shneider *et al*, 2013; Alcoforado Diniz & Coulthurst, 2015; Liang *et al*, 2015; Unterweger *et al*, 2015; Bondage *et al*, 2016). Tle1 binds to three different regions of VgrG (bottom, centre and top), and the three Tle1 molecules are located on the side of the needle rather than on its tip. This contrasts with the position of PAAR-fused Tse6 effector/adaptor in the *P. aeruginosa* VgrG tip complex EM structure (Whitney *et al*, 2015; Quentin *et al*, 2018; Fig EV3B and E). Tle1 positioning on the VgrG sides and the multiple attachment zones tightly tether Tle1 to the spike, which will be released by some unknown mechanism in the periplasm of the target cell. The non-covalent nature of the bonds may also allow Tle1 to be separated from the VgrG spike to elicit its function. The oxidative nature of the periplasm or the presence of specific chaperones might provide the source for Tle1 dissociation. Further work will need to be carried out to understand the implication of such flexible interactions in VgrG–Tle1 dissociation.

The EAEC T6SS-1 cluster also encodes a PAAR protein downstream the Tli1 immunity-encoding gene. However, in the VgrG–Tle1 complex characterized here, no PAAR is needed for the three Tle1 proteins to bind to the VgrG trimeric spike. The tip of the needle is free to accommodate a PAAR protein necessary for target cell penetration. In the future, it would be of particular interest to co-purify and image PAAR associated with the VgrG–Tle1 complex.

In contrast to canonical VgrGs, such as VgrG^{PA}, VgrG^{EAEC} bears a C-terminal extension (CTD) comprising DUF2345 and TTR domains, linked to the gp27/gp5 base by two long helices (Fig 2G). As shown in this study, the DUF2345 domain folds as a β-prism and hence extends the length of the VgrG^{EAEC} gp5-like β-helix. This extension, as well as the TTR domain, corresponds to the major binding regions of Tle1. VgrG^{EAEC} is therefore a fusion between a prototypical VgrG and DUF2345/TTR extensions that serve as internal adaptor domains (Bondage *et al*, 2016; Flaugnatti *et al*, 2016; Wettstadt *et al*, 2019). However, there is an additional contact between Tle1 and the base of gp5-C domain of VgrG. The direct binding of Tle1 on VgrG^{EAEC} therefore represents the first report of a new mode of effector loading on the T6SS spike. Similar modes of binding might be predicted. This organization of VgrG C-terminal extension (i.e. the presence of two long helices followed by the DUF2345 and the TTR domains) corresponds to the COG4532 found at the C-terminal domain of a subgroup of VgrG proteins in Proteobacteria (Boyer *et al*, 2009). This group includes proteins such as the VgrG encoded upstream of a putative Tle3 effector in uropathogenic *E. coli* CFT073, or VgrG2a from *P. aeruginosa* encoded upstream the Tle4-like *tlpE* effector (Wood *et al*, 2019; Appendix Fig S7). The structural organization of these VgrG proteins and their genetic link to phospholipase-encoding genes suggest that these phospholipases might also be directly recruited to the spike extension for delivery.

Tle1 inhibition by VgrG

It is noteworthy that the 3' of the *vgrG* gene overlaps with the *tle1* 5' in EAEC (Flaugnatti *et al*, 2016), suggesting translational coupling of the VgrG and Tle1 proteins, a mechanism that evolved to promote protein stabilization or to prevent protein toxicity. Indeed, our results show that the VgrG-bound Tle1 phospholipase is inactive as the catalytic site of Tle1 is masked by the mode of binding to VgrG. Production of the Tle1 phospholipase may have a deleterious effect on the cytoplasmic membrane phospholipids, and VgrG-mediated inhibition could be regarded as a surveillance mechanism to prevent phospholipid degradation in the attacker cell. However, previous results have shown that Tle1 cytoplasmic overproduction has no impact on the growth of *E. coli* K-12 cells (Flaugnatti *et al*, 2016). Another hypothesis is that there is no need to inhibit Tle1 but rather a need to protect the catalytic site and to prevent exposition of the hydrophobic entrance. Nevertheless, Tle1 needs to dissociate from VgrG once in the periplasm of the target cell.

In conclusion, we have identified a novel mechanism of loading and inhibition in the T6SS Tle1 toxin that establishes a new relationship between the spike and its carrier effector.

Materials and Methods

Bacterial strains, growth conditions and chemicals

Strains used in this study are listed in Appendix Table S1. *Escherichia coli* DH5 α , BL21(DE3) and W3110 were used for cloning procedures, protein production and co-immunoprecipitation, respectively. EAEC strain 17-2 and its isogenic derivatives were used for *in vivo* studies. Cells were grown at 37°C with aeration in LB or in T6SS-1-inducing medium (Brunet *et al*, 2011) [SIM; M9 minimal medium, 0.2% glycerol, 1 μ g/ml vitamin B1, 100 μ g/ml casamino acids, 10% LB, supplemented or not with 1.5% Bacto agar, ampicillin (100 μ g/ml), kanamycin (50 μ g/ml) or chloramphenicol (30 μ g/ml)]. Gene expression from pBAD (Guzman *et al*, 1995) and pOK12 (Vieira & Messing, 1991) derivatives was induced by the addition of 0.02–0.2% of L-arabinose (Sigma-Aldrich) and 100 μ M isopropyl-thio- β -D-galactopyranoside (IPTG; Eurobio), respectively. Gene expression from pETDuet-1 and pRSFDuet-1 (Novagen) derivative vectors was induced by the addition of 1 mM IPTG.

Cloning procedures

The plasmids and primers used in this study are listed in Appendix Table S1. PCRs were performed using a Biometra thermocycler using the Q5 high-fidelity DNA polymerase (New England Biolabs) and EAEC 17-2 chromosomal DNA as a template. Custom oligonucleotides (Sigma-Aldrich) are listed in Appendix Table S1. pRSF-Tle1^H and pET-^SVgrG were constructed by a restriction–ligation procedure. The sequence encoding Tle1 was amplified by PCR using 5-NdeI-Tle1 and 3-FseI-Tle1^H primers introducing NdeI and FseI sites, respectively, and cloned into the pRSFDuet-1 (Novagen) multiple cloning site 2 (MCS2) to yield pRSF-Tle1^H. The 3-FseI-Tle1^H primer introduces a sequence encoding a 6×His-tag to allow in-frame fusion of Tle1 with a C-terminal hexa-histidine extension. The sequence encoding VgrG was amplified by PCR using primers 5-BamHI-^SVgrG

and 3-HindIII-VgrG introducing BamHI and HindIII sites, respectively, and cloned into the pETDuet-1 MCS1 to yield pET-^SVgrG. The 5-BamHI-^SVgrG primer introduces a sequence encoding a Strep-tagII to allow in-frame fusion of VgrG with an N-terminal Strep-tagII. The same cloning strategy was used for pET-^SVgrG_{ACTD} and pET-^SVgrG_{1–490}, with the use of primers 5-BamHI-^SVgrG and 3-HindIII-VgrG_{ACTD} for pET-^SVgrG_{ACTD}, and primers 5-BamHI-^SVgrG and 3-HindIII-VgrG_{1–490} for pET-^SVgrG_{1–490}. For pBAD18-Tle1 Δ 1–26_{VSVG}, pBAD18-Tle1 Δ 1–34_{VSVG} and pRSF-Tle1 Δ 1–26^H constructions, the sequence encoding amino acids 1–26 (or 1–34) of Tle1 has been deleted from pBAD18-Tle1_{VSVG} (Flaugnatti *et al*, 2016) or pRSF-Tle1^H by QuikChange PCR-based targeted mutagenesis using complementary pairs of oligonucleotides and the PfuTurbo high-fidelity polymerase (Agilent Technologies). Similarly, the K28-to-E/K29-to-E/K30-to-E substitutions were introduced in the pBAD18-Tle1_{VSVG} plasmid by QuikChange PCR-based targeted mutagenesis. All constructs were verified by restriction analysis and DNA sequencing (Eurofins, MWG).

Antibacterial competition assay

Antibacterial competition assays were performed as described previously (Flaugnatti *et al*, 2016), using wild-type *E. coli* W3110 cells transformed with the pUA66-*rrnB* plasmid (Zaslaver *et al*, 2006) as a prey. In addition to conferring resistance to kanamycin, the pUA66-*rrnB* plasmid allows a strong constitutive expression of the green fluorescent protein. The experiments were done in triplicate, with identical results, and the results of a representative experiment are shown here.

Co-immunoprecipitation

W3110 cells producing Tle1, Tle1 Δ 1–26 or VgrG proteins from independent plasmids were subjected to co-immunoprecipitation using ANTI-FLAG[®] M2 affinity gel (Sigma-Aldrich), as described previously (Flaugnatti *et al*, 2016). Anti-FLAG (clone M2; Sigma-Aldrich) or anti-VSV-G (clone P5D4; Sigma-Aldrich) monoclonal antibody was used for Western blot analyses.

VgrG–Tle1 complex production and co-purification

The pRSF-Tle1^H and pET-^SVgrG plasmids were co-transformed into BL21(DE3). Following growth at 37°C in LB medium to an OD_{600 nm} of 0.7, the expression of *tle1* and *vgrG* genes was induced with 1 mM IPTG at 16°C for 16 h. Cells were pelleted, resuspended in lysis buffer (50 mM Tris–HCl pH 8.0, 150 mM NaCl, 1 mM EDTA, 100 μ g/ml DNase I, 100 μ g/ml lysozyme, cComplete EDTA-free protease inhibitor cocktail (Sigma) and 10 mM MgCl₂) and broken using an Emulsiflex-C5 (Avestin). After centrifugation at 38,500 \times g for 30 min, the supernatant was loaded onto a 5-ml StrepTrap HP column (GE Healthcare) at 4°C, and the column was washed with affinity buffer (50 mM Tris–HCl pH 8.0, 150 mM NaCl) at 4°C. The ^SVgrG–Tle1^H complex was then eluted directly into a 5-ml HisTrap HP column (GE Healthcare) with affinity buffer containing 2.5 mM desthiobiotin (IBA). After a washing step in affinity buffer supplemented with 20 mM imidazole, the ^SVgrG–Tle1^H complex was eluted in affinity buffer supplemented with 500 mM imidazole. The fractions corresponding to the peak were pooled and loaded onto a Superose 6 10/300 column (GE Healthcare) equilibrated in a buffer

containing 50 mM HEPES pH 7.5 and 150 mM NaCl. The $^{\text{S}}\text{VgrG}$ – Tle1^{H} complex was eluted as a single monodisperse peak. The same production conditions and purification protocol were applied for the purification of $^{\text{S}}\text{VgrG}$, $^{\text{S}}\text{VgrG}_{1-490}$, Tle1^{H} and $\text{Tle1}_{\Delta 1-26}$, except that only one affinity column was performed (StrepTrap HP for $^{\text{S}}\text{VgrG}$ and $^{\text{S}}\text{VgrG}_{1-490}$; HisTrap for Tle1^{H} and $\text{Tle1}_{\Delta 1-26}$) followed by a gel filtration as described above. For Tle1 inhibition studies, $^{\text{S}}\text{VgrG}$ and $^{\text{S}}\text{VgrG}_{1-490}$ eluted from the StrepTrap column were used directly (without a gel filtration step), due to the tendency of $^{\text{S}}\text{VgrG}$ to precipitate during or after the gel filtration step when purified alone. A representative SDS–PAGE followed by InstantBlue staining of the resulting purified proteins is presented in Fig 5C.

SYPRO Ruby staining

Aliquots of 2.5, 5 and 10 μl of the VgrG – Tle1 complex from two different peak fractions of the gel filtration column were subjected to SDS–PAGE. The gel was then stained with SYPRO Ruby as recommended by the manufacturer (Invitrogen). Protein bands were visualized using a Bio-Rad ChemiDoc MP Imaging System, using a 605/50 Filter (excitation wavelength = 488 nm, emission wavelength = 605 nm) with 0.5-s exposition, and the fluorescence intensity was quantified using the Fuji Image software. Intensities were divided by the molecular weight of each protein, and the quantification is expressed as the mean \pm standard deviation relative to VgrG band intensity.

Cryo-EM sample preparation and data collection

UltraAuFoil Holey Gold Film grids (Quantifoil) were glow-discharged for 20 s at 2 mA in an ELMO glow discharge cleaning system (Agar Scientific, UK). Four microlitres of sample at 600 $\mu\text{g}/\text{ml}$ was loaded on the glow-discharged grid at 100% humidity and 4°C in a Vitrobot (Thermo Fisher Scientific, USA). Following a 5-s pre-blot, the grid was blotted for 4 s and plunged into liquid ethane. Grids were screened on a Talos Arctica electron microscope equipped with a Falcon 3EC camera (Thermo Fisher Scientific, USA), and the final data were collected on a K2 Summit detector through a Gatan Quantum 967 LS energy filter using a 20 eV slit width in zero-loss mode (Gatan, Japan) on a Titan Krios transmission electron microscope at 300 kV (Thermo Fisher Scientific, USA). Table 2 summarizes the acquisition parameters.

Cryo-EM data processing

The 40 frames for each movie collected were aligned for each of the 11,600 movies using MotionCor2, binned by 1.28 with dose weighting (1.24 e $^{-}/\text{\AA}^2/\text{frame}$) and with 5×5 patches applied (Zheng *et al.*, 2017). gCTF was used to estimate the CTF parameters (Zhang, 2016). cryoSPARC (Punjani *et al.*, 2017) template picker selected 1.94 million particles that were extracted with a box size of 350 pix. After several rounds of 2D classification in cryoSPARC (Fig EV2A), a heterogeneous *ab initio* reconstruction with two classes and a heterogeneous refinement (two classes), 468,438 particles were selected for homogeneous refinement. An initial unmasked refinement using the *ab initio* model from the cryoSPARC gave us a resolution of 2.7 \AA with no applied symmetry (Fig EV2B–D). A masked local refinement around the physiological complex yielded a final

Table 2. Cryo-EM data acquisition and analysis parameters.

	VgrG–Tle (EMD-10218) (PDB 6SJL)	VgrG (EMD-10219) (PDB 6SKO)	Tle–TTR (EMD-10225) (PDB 6SKI)
<i>Data collection and processing</i>			
Magnification	165,000 \times	165,000 \times	165,000 \times
Voltage (kV)	300	300	300
Electron exposure (e $^{-}/\text{\AA}^2$)	53.94	53.94	53.94
Defocus range (μm)	0.5–2	0.5–2	0.5–2
Pixel size (\AA)	0.85	0.85	0.85
Spot size	9	9	9
Symmetry imposed	C1	C1	C1
Number of images	11,670	11,670	11,670
Initial particle images (no.)	1,942,084	1,942,084	1,942,084
Final particle images (no.)	468,438	468,438	468,438
Map resolution (\AA)	2.6 (2.9)	2.26 (2.7)	2.55 (2.8)
FSC threshold	0.143 (0.5)	0.143 (0.5)	0.143 (0.5)
Map resolution range (\AA)	2.2–15	2.15–2.48	2.25–7
Binning	1.28	1.28	1.28
<i>Refinement</i>			
Initial model used (PDB code)	N/A	N/A	N/A
Model resolution (\AA)	2.6 (2.7)	2.1 (2.2)	2.6 (2.7)
FSC threshold	0.143 (0.5)	0.143 (0.5)	0.143 (0.5)
Map sharpening <i>B</i> -factor (\AA^2)	84.99	66.07	75.21
<i>Model composition</i>			
Number of chains	6	3	2
Non-hydrogen atoms	19,460	5,890	4,434
Protein residues	2,537	801	569
Ligands	0	0	0
<i>B</i> -factors (\AA^2)			
Protein (min/max)	25.27/157.57	34.83/63.05	40.72/92.41
Ligand	N/A	N/A	N/A
<i>R.m.s. deviations</i>			
Bond lengths (\AA)	0.013	0.008	0.004
Bond angles ($^{\circ}$)	0.855	0.726	0.713
<i>Validation</i>			
MolProbity score	2.02	1.70	1.55
Clashscore	12.96	9.23	8.64
Poor rotamers (%)	0.05	0.97	1.29
<i>Ramachandran plot</i>			
Favoured (%)	94.06	96.69	98.38
Allowed (%)	5.74	3.31	1.62
Disallowed (%)	0.20	0	0

resolution of 2.6 Å (Fig EV2E). The density corresponding to the Tle1 effector was refined locally with cryoSPARC to a resolution of 2.5 Å. In Relion, CTF Refine and the Bayesian polishing steps (Zivanov *et al*, 2019) yielded a final resolution of 2.3 Å for the masked VgrG density and were used for model building and real space refinement (Fig EV2F and G). The quality of the maps for the Tle1/TTR densities was worse than that obtained with cryoSPARC and was thus not used. The resolution for the Tle1 and VgrG densities was calculated by cryoSPARC and Relion postprocess, respectively, according to the “gold standard” method using 0.143 as the FSC value cut-off (Rosenthal & Henderson, 2003). The local resolution was calculated by cryoSPARC (Punjani *et al*, 2017) or Relion with a cut-off of 0.5 (Appendix Fig S5A–C).

Model building and validation

Model building proceeded differently for VgrG and Tle1, but for both, no homologous protein could be docked in the density and the Phenix autosharpened (Terwilliger *et al*, 2018b) cryo-EM densities were used. For Tle1, a partial initial model based on the primary sequence was built using phenix.map_to_model (Terwilliger *et al*, 2018a). The model was subsequently corrected and extended manually in Coot (Emsley *et al*, 2010). For VgrG, the Phenix automatic model building was not successful. The model was built starting with the only 2 α -helices and using the cryo-EM density to place manually all the amino acid sequence. For the TTR domain that interacts with Tle1, we combined the use of bulky side chains as guides for model building, secondary structure and residue contact predictions according to the Phyre2 (Kelley *et al*, 2015) and RaptorX (Källberg *et al*, 2012) servers, respectively. The VgrG models were both refined using phenix.real_space_refine (Afonine *et al*, 2018), and manual adjustments were done with Coot 0.9 (Emsley *et al*, 2010). Each model was initially validated using the protocol implemented in Refmac5 (Murshudov *et al*, 2011) and visually (Appendix Fig S8). The FSC map-to-model was calculated with the autosharpened maps (FSC_{sum}). The model was shaken by 0.5 Å, and the FSC map-to-model was calculated with one Half map (FSC_{work}). This refined model was then used to calculate the FSC map-to-model with the other Half map (FSC_{free}) (Appendix Fig S8A–C). The cross-correlation between each amino acid in the model and map and the MolProbity score (Chen *et al*, 2010) were calculated using phenix.real_space_refine (Afonine *et al*, 2018; Appendix Fig S9, Table 2). Pore radius calculations were carried out using the MOLE server (Berka *et al*, 2012), and the protein interfaces were analysed with PISA (Krissinel & Henrick, 2007). Unless stated otherwise, all of the figures were generated either using Chimera (Pettersen *et al*, 2004), ChimeraX (Goddard *et al*, 2018) or Coot (Emsley *et al*, 2010).

Cross-linking mass spectrometry

Cross-linking of the purified complexes was carried out with freshly prepared NNP9 (10 mM in DMSO) using 10:1 cross-linker/protein molar ratio. Cross-linking was performed at 4°C for 30 min and stopped by the addition of ammonium bicarbonate (AB, final concentration 50 mM) for 15 min at 4°C. The samples were transferred into a molecular filter device (Amicon Ultra 0.5 ml with 30 kDa molecular cut-off) and centrifuged at 10,000 × g for 5 min. The concentrate was then washed four times by concentration–

dilution cycle with AB 50 mM to remove the excess of cross-linker. The labelled protein was digested overnight at 37°C by addition of Trypsin Gold, Mass Spectrometry Grade (Promega) at an enzyme:protein ratio of 1:50 (w:w) under 900-rpm shaking. The peptides were recovered through the molecular filtering device by centrifugation. 50 μ l of 0.1% (v:v) formic acid was added onto the filter, and a second centrifugation was performed to improve the peptide recovery. Cross-linked protein digests were analysed by nanoLC-MS/MS on an Orbitrap Q Exactive Plus mass spectrometer (Thermo Scientific). Briefly, peptides were separated on homemade C18 column using a 90-min water/acetonitrile gradient. The 10 most intense ions with at least three charges were selected for HCD fragmentation (NCE 24). NanoLC-MS/MS data were processed automatically using Mass Spec Studio v2.0 (Sarpe *et al*, 2016) with methionine oxidation as a variable modification and NNP9 modification sites: lysine, serine, threonine and tyrosine. Mass modifications were set to 314.1127 Da for cross-linked peptides and 288.1335 and 331.1393 for dead-end modifications when NNP9 reacted respectively with water or ammonium molecule. Cross-linked peptides were searched using the parameter file provided in supplemental data (Dataset EV2). MS/MS spectra of all cross-linked candidates were further manually checked to confirm their identification. Experiments were performed in duplicate (using two different complex preparations), and only cross-linked peptides identified in both experiments were considered.

Phospholipase A1 fluorescent assays

PLA1 activities of Tle1, Tle1 Δ_{1-26} , VgrG and the VgrG–Tle1 complex were monitored using BODIPYVR dye-labelled phospholipids: PED-A1 (N-((6-(2,4-DNP)Amino)Hexanoyl)-(BODIPYVRFL C5)-2-Hexyl-sn-Glycero-3-Phosphoethanolamine) (Farber, 2001; Darrow *et al*, 2011), as described previously (Flaughnatti *et al*, 2016). Enzyme activities were assayed at room temperature in 50 mM HEPES pH 7.5 and 150 mM NaCl for 25 min in a final volume of 200 μ l containing 5 μ M of the substrate and 1.18 μ M of Tle1^H, 1.18 μ M of ^SVgrG or 0.393 μ M of ^SVgrG–Tle1^H complex (corresponding to 1.18 μ M of Tle1 considering a 3:3 stoichiometry) purified proteins (from 1 to 2 mg/ml stock solutions). *Thermomyces lanuginosus* lipase (TLL; Sigma-Aldrich) was used as a positive control for PLA1 activity. Inhibition assays were performed in desthiobiotin-containing buffer (Tris–HCl 50 mM pH 8.0, NaCl 150 mM, desthiobiotin 2.5 mM) using ^SVgrG or ^SVgrG_{1–490} purified at 1.5–2 mg/ml, after checking that desthiobiotin did not affect Tle1 PLA1 activity. Lysozyme from chicken egg white (Sigma) was used as a negative control. Differences in Tle1 activities between groups were examined by unpaired two-sample Fisher–Pitman permutation test.

Computer algorithms

EAEC Tle1 orthologs (EC042_4534; NCBI Gene Identifier (GI): 284924255) were detected using BlastP analysis against the KEGG GENES database and aligned using ClustalW and draw alignment tool in KEGG (Kanehisa *et al*, 2017), or Multalin (Corpet, 1988; Robert & Gouet, 2014). Protein domains were identified using Pfam (Sonnhammer *et al*, 1997) or CDart (Geer *et al*, 2002).

Expanded View for this article is available online.

Acknowledgements

We thank the members of the Cascales, Lloubès, Bouveret and Sturgis groups for discussions; Artemis Kosta for EM assistance; and Moly Ba, Isabelle Bringer, Annick Brun, and Olivier Uderso for technical assistance. This work has benefited from the facilities and expertise of the Biophysical and Structural Chemistry Platform (BPCS) at IECB, CNRS UMS3033, Inserm US001, Bordeaux University; in particular, we would like to thank Armel Bezault. The authors acknowledge the use of resources of the cryo-electron microscopy service platform at the EMBL Heidelberg and the support of Felix Weis for data collection. The access to the facility has been supported by iNEXT, Grant Number 653706, funded by the Horizon 2020 programme of the European Commission. This work was supported by the Centre National de la Recherche Scientifique (CNRS), Aix-Marseille Université and grants from the Agence Nationale de la Recherche (ANR-14-CE14-0006-02 and ANR-18-CE15-0013-01). NF was supported by the ANR-14-CE14-0006-02 grant. The work of ED is supported by the Institut National de la Santé et de la Recherche Médicale (INSERM). The work of MR is supported by the Institut Pasteur, the CNRS and the Projet d'Investissement d'Avenir BIP:BIP (ANR-10-BINF-03-13).

Author contributions

NF, CR, MR, ED, JC-R, RF and LJ designed research. NF, CR, MR, SGB, VAN and LJ performed research. MR, SC, JC-R, RF and EC provided tools. NF, CR, MR, SGB, ED, SC, EC, RF and LJ analysed the data. NF, CR, RF and LJ wrote the paper with contributions from MR, JC-R and EC.

Conflict of interest

The authors declare that they have no conflict of interest.

References

- Afonine PV, Poon BK, Read RJ, Sobolev OV, Terwilliger TC, Urzhumtsev A, Adams PD (2018) Real-space refinement in PHENIX for cryo-EM and crystallography. *Acta Crystallogr Sect D Struct Biol* 74: 531–544
- Alcoforado Diniz J, Coulthurst SJ (2015) Intraspecies competition in *Serratia marcescens* is mediated by type VI-secreted Rhs effectors and a conserved effector-associated accessory protein. *J Bacteriol* 197: 2350–2360
- Basler M, Pilhofer M, Henderson GP, Jensen GJ, Mekalanos JJ (2012) Type VI secretion requires a dynamic contractile phage tail-like structure. *Nature* 483: 182–186
- Berka K, Hanak O, Sehnal D, Banas P, Navratilova V, Jaiswal D, Ionescu C-M, Svobodova Varekova R, Koca J, Otyepka M (2012) MOLEonline 2.0: interactive web-based analysis of biomacromolecular channels. *Nucleic Acids Res* 40: W222–W227
- Blondel CJ, Jiménez JC, Contreras I, Santiviago CA (2009) Comparative genomic analysis uncovers 3 novel loci encoding type six secretion systems differentially distributed in *Salmonella* serotypes. *BMC Genom* 10: 354
- Bondage DD, Lin J-S, Ma L-S, Kuo C-H, Lai E-M (2016) VgrG C terminus confers the type VI effector transport specificity and is required for binding with PAAR and adaptor-effector complex. *Proc Natl Acad Sci USA* 113: E3931–E3940
- Boyer F, Fichant G, Berthod J, Vandenbrouck Y, Attree I (2009) Dissecting the bacterial type VI secretion system by a genome wide in silico analysis: what can be learned from available microbial genomic resources? *BMC Genom* 10: 104
- Brooks TM, Unterwieser D, Bachmann V, Kostiuik B, Pukatzki S (2013) Lytic activity of the *Vibrio cholerae* Type VI secretion toxin VgrG-3 is inhibited by the antitoxin TsaB. *J Biol Chem* 288: 7618–7625
- Brunet YR, Bernard CS, Gavioli M, Lloubès R, Cascales E (2011) An epigenetic switch involving overlapping fur and DNA methylation optimizes expression of a type VI secretion gene cluster. *PLoS Genet* 7: e1002205
- Brunet YR, Zoued A, Boyer F, Douzi B, Cascales E (2015) The type VI secretion TssEFGK-VgrG phage-like baseplate is recruited to the TssJLM membrane complex via multiple contacts and serves as assembly platform for tail tube/sheath polymerization. *PLoS Genet* 11: e1005545
- Chen VB, Arendall WB, Headd JJ, Keedy DA, Immormino RM, Kapral GJ, Murray LW, Richardson JS, Richardson DC (2010) MolProbity: all-atom structure validation for macromolecular crystallography. *Acta Crystallogr Sect D Biol Crystallogr* 66: 12–21
- Cherrak Y, Rapisarda C, Pellarin R, Bouveret G, Bardiaux B, Allain F, Malosse C, Rey M, Chamot-Rooke J, Cascales E et al (2018) Biogenesis and structure of a type VI secretion baseplate. *Nat Microbiol* 3: 1404–1416
- Cianfanelli FR, Monlezun L, Coulthurst SJ (2016) Aim, load, fire: the type VI secretion system, a bacterial nanoweapon. *Trends Microbiol* 24: 51–62
- Corpet F (1988) Multiple sequence alignment with hierarchical clustering. *Nucleic Acids Res* 16: 10881–10890
- Darrow AL, Olson MW, Xin H, Burke SL, Smith C, Schalk-Hihi C, Williams R, Bayoumy SS, Deckman IC, Todd MJ et al (2011) A novel fluorogenic substrate for the measurement of endothelial lipase activity. *J Lipid Res* 52: 374–382
- Dong TG, Ho BT, Yoder-Himes DR, Mekalanos JJ (2013) Identification of T6SS-dependent effector and immunity proteins by Tn-seq in *Vibrio cholerae*. *Proc Natl Acad Sci USA* 110: 2623–2628
- Durand E, Cambillau C, Cascales E, Journet L (2014) VgrG, Tae, Tle, and beyond: the versatile arsenal of type VI secretion effectors. *Trends Microbiol* 22: 498–507
- Durand E, Nguyen VS, Zoued A, Logger L, Péhau-Arnaudet G, Aschtgen M-S, Spinelli S, Desmyter A, Bardiaux B, Dujeancourt A et al (2015) Biogenesis and structure of a type VI secretion membrane core complex. *Nature* 523: 555–560
- Emsley P, Lohkamp B, Scott WG, Cowtan K (2010) Features and development of Coot. *Acta Crystallogr Sect D Biol Crystallogr* 66: 486–501
- Farber SA (2001) Genetic analysis of digestive physiology using fluorescent phospholipid reporters. *Science* 292: 1385–1388
- Flaugnatti N, Le TTH, Canaan S, Aschtgen M-S, Nguyen VS, Blangy S, Kellenberger C, Roussel A, Cambillau C, Cascales E et al (2016) A phospholipase A 1 antibacterial Type VI secretion effector interacts directly with the C-terminal domain of the VgrG spike protein for delivery. *Mol Microbiol* 99: 1099–1118
- Geer LY, Domrachev M, Lipman DJ, Bryant SH (2002) CDART: protein homology by domain architecture. *Genome Res* 12: 1619–1623
- Goddard TD, Huang CC, Meng EC, Pettersen EF, Couch GS, Morris JH, Ferrin TE (2018) UCSF ChimeraX: meeting modern challenges in visualization and analysis. *Protein Sci* 27: 14–25
- Guzman LM, Belin D, Carson MJ, Beckwith J (1995) Tight regulation, modulation, and high-level expression by vectors containing the arabinose PBAD promoter. *J Bacteriol* 177: 4121–4130
- Hachani A, Wood TE, Filloux A (2016) Type VI secretion and anti-host effectors. *Curr Opin Microbiol* 29: 81–93
- Ho BT, Dong TG, Mekalanos JJ (2014) A view to a kill: the bacterial type VI secretion system. *Cell Host Microbe* 15: 9–21
- Hu H, Zhang H, Gao Z, Wang D, Liu G, Xu J, Lan K, Dong Y (2014) Structure of the type VI secretion phospholipase effector Tle1 provides insight into its hydrolysis and membrane targeting. *Acta Crystallogr Sect D Biol Crystallogr* 70: 2175–2185
- Källberg M, Wang H, Wang S, Peng J, Wang Z, Lu H, Xu J (2012) Template-based protein structure modeling using the RaptorX web server. *Nat Protoc* 7: 1511–1522

- Kanamaru S, Leiman PG, Kostyuchenko VA, Chipman PR, Mesyanzhinov VV, Arisaka F, Rossmann MG (2002) Structure of the cell-puncturing device of bacteriophage T4. *Nature* 415: 553–557
- Kanehisa M, Furumichi M, Tanabe M, Sato Y, Morishima K (2017) KEGG: new perspectives on genomes, pathways, diseases and drugs. *Nucleic Acids Res* 45: D353–D361
- Kelley LA, Mezulis S, Yates CM, Wass MN, Sternberg MJE (2015) The Phyre2 web portal for protein modeling, prediction and analysis. *Nat Protoc* 10: 845–858
- Krissinel E, Henrick K (2007) Inference of macromolecular assemblies from crystalline state. *J Mol Biol* 372: 774–797
- Leiman PG, Basler M, Ramagopal UA, Bonanno JB, Sauder JM, Pukatzki S, Burley SK, Almo SC, Mekalanos JJ (2009) Type VI secretion apparatus and phage tail-associated protein complexes share a common evolutionary origin. *Proc Natl Acad Sci USA* 106: 4154–4159
- Liang X, Moore R, Wilton M, Wong MJQ, Lam L, Dong TG (2015) Identification of divergent type VI secretion effectors using a conserved chaperone domain. *Proc Natl Acad Sci USA* 112: 9106–9111
- Logger L, Aschtgen M-S, Guérin M, Cascales E, Durand E (2016) Molecular dissection of the interface between the type VI secretion TssM cytoplasmic domain and the TssG baseplate component. *J Mol Biol* 428: 4424–4437
- Ma J, Pan Z, Huang J, Sun M, Lu C, Yao H (2017) The Hcp proteins fused with diverse extended-toxin domains represent a novel pattern of antibacterial effectors in type VI secretion systems. *Virulence* 8: 1189–1202
- Murshudov GN, Skubák P, Lebedev AA, Pannu NS, Steiner RA, Nicholls RA, Winn MD, Long F, Vagin AA (2011) REFMAC 5 for the refinement of macromolecular crystal structures. *Acta Crystallogr Sect D Biol Crystallogr* 67: 355–367
- Nazarov S, Schneider JP, Brackmann M, Goldie KN, Stahlberg H, Basler M (2018) Cryo-EM reconstruction of type VI secretion system baseplate and sheath distal end. *EMBO J* 37: e97103
- Nguyen VS, Logger L, Spinelli S, Legrand P, Huyen Pham TT, Nhung Trinh TT, Cherrak Y, Zoued A, Desmyter A, Durand E et al (2017) Type VI secretion TssK baseplate protein exhibits structural similarity with phage receptor-binding proteins and evolved to bind the membrane complex. *Nat Microbiol* 2: 17103
- Nury C, Redeker V, Dautrey S, Romieu A, van der Rest G, Renard P-Y, Melki R, Chamot-Rooke J (2015) A novel bio-orthogonal cross-linker for improved protein/protein interaction analysis. *Anal Chem* 87: 1853–1860
- Pettersen EF, Goddard TD, Huang CC, Couch GS, Greenblatt DM, Meng EC, Ferrin TE (2004) UCSF Chimera—a visualization system for exploratory research and analysis. *J Comput Chem* 25: 1605–1612
- Pukatzki S, Ma AT, Sturtevant D, Krastins B, Sarracino D, Nelson WC, Heidelberg JF, Mekalanos JJ (2006) Identification of a conserved bacterial protein secretion system in *Vibrio cholerae* using the *Dictyostelium* host model system. *Proc Natl Acad Sci USA* 103: 1528–1533
- Punjani A, Rubinstein JL, Fleet DJ, Brubaker MA (2017) cryoSPARC: algorithms for rapid unsupervised cryo-EM structure determination. *Nat Methods* 14: 290–296
- Quentin D, Ahmad S, Shanthamoorthy P, Mougous JD, Whitney JC, Raunser S (2018) Mechanism of loading and translocation of type VI secretion system effector Tse6. *Nat Microbiol* 3: 1142–1152
- Rapisarda C, Cherrak Y, Kooger R, Schmidt V, Pellarin R, Logger L, Cascales E, Pilhofer M, Durand E, Fronzes R (2019) In situ and high-resolution cryo-EM structure of a bacterial type VI secretion system membrane complex. *EMBO J* 38: e100886
- Robert X, Gouet P (2014) Deciphering key features in protein structures with the new ENDscript server. *Nucleic Acids Res* 42: W320–W324
- Rosenthal PB, Henderson R (2003) Optimal determination of particle orientation, absolute hand, and contrast loss in single-particle electron cryomicroscopy. *J Mol Biol* 333: 721–745
- Russell AB, Peterson SB, Mougous JD (2014) Type VI secretion system effectors: poisons with a purpose. *Nat Rev Microbiol* 12: 137–148
- Sarpe V, Rafiei A, Hepburn M, Ostan N, Schryvers AB, Schriemer DC (2016) High sensitivity crosslink detection coupled with integrative structure modeling in the mass spec studio. *Mol Cell Proteomics* 15: 3071–3080
- Shneider MM, Buth SA, Ho BT, Basler M, Mekalanos JJ, Leiman PG (2013) PAAR-repeat proteins sharpen and diversify the type VI secretion system spike. *Nature* 500: 350–353
- Silverman JM, Agnello DM, Zheng H, Andrews BT, Li M, Catalano CE, Gonen T, Mougous JD (2013) Haemolysin coregulated protein is an exported receptor and chaperone of Type VI secretion substrates. *Mol Cell* 51: 584–593
- Sonnhammer ELL, Eddy SR, Durbin R (1997) Pfam: a comprehensive database of protein domain families based on seed alignments. *Proteins Struct Funct Genet* 28: 405–420
- Spínola-Amilibia M, Davó-Siguero I, Ruiz FM, Santillana E, Medrano FJ, Romero A (2016) The structure of VgrG1 from *Pseudomonas aeruginosa*, the needle tip of the bacterial type VI secretion system. *Acta Crystallogr Sect D Struct Biol* 72: 22–33
- Suarez G, Sierra JC, Erova TE, Sha J, Horneman AJ, Chopra AK (2010) A type VI secretion system effector protein, VgrG1, from *Aeromonas hydrophila* that induces host cell toxicity by ADP ribosylation of actin. *J Bacteriol* 192: 155–168
- Taylor NMI, Prokhorov NS, Guerrero-Ferreira RC, Shneider MM, Browning C, Goldie KN, Stahlberg H, Leiman PG (2016) Structure of the T4 baseplate and its function in triggering sheath contraction. *Nature* 533: 346–352
- Terwilliger TC, Adams PD, Afonine PV, Sobolev OV (2018a) A fully automatic method yielding initial models from high-resolution cryo-electron microscopy maps. *Nat Methods* 15: 905–908
- Terwilliger TC, Sobolev OV, Afonine PV, Adams PD (2018b) Automated map sharpening by maximization of detail and connectivity. *Acta Crystallogr Sect D Struct Biol* 74: 545–559
- Uchida K, Leiman PG, Arisaka F, Kanamaru S (2014) Structure and properties of the C-terminal β -helical domain of VgrG protein from *Escherichia coli* O157. *J Biochem* 155: 173–182
- Unterwiesing D, Kostiuk B, Ojtjengerdes R, Wilton A, Diaz-Satizabal L, Pukatzki S (2015) Chimeric adaptor proteins translocate diverse Type VI secretion system effectors in *Vibrio cholerae*. *EMBO J* 34: 2198–2210
- Vieira J, Messing J (1991) New pUC-derived cloning vectors with different selectable markers and DNA replication origins. *Gene* 100: 189–194
- Wettstadt S, Wood TE, Fecht S, Filloux A (2019) Delivery of the *Pseudomonas aeruginosa* phospholipase effectors PlcA and PlcB in a VgrG- and H2-T6SS-dependent manner. *Front Microbiol* 10: 1718
- Whitney JC, Quentin D, Sawai S, LeRoux M, Harding BN, Ledvina HE, Tran BQ, Robinson H, Goo YA, Goodlett DR et al (2015) An interbacterial NAD (P) + glycohydrolase toxin requires elongation factor Tu for delivery to target cells. *Cell* 163: 607–619
- Wood TE, Howard SA, Wettstadt S, Filloux A (2019) PAAR proteins act as the ‘sorting hat’ of the Type VI secretion system. *Microbiology* 165: 1203–1218
- Zaslaver A, Bren A, Ronen M, Itzkovitz S, Kikoin I, Shavit S, Liebermeister W, Surette MG, Alon U (2006) A comprehensive library of fluorescent transcriptional reporters for *Escherichia coli*. *Nat Methods* 3: 623–628
- Zhang K (2016) Gctf: real-time CTF determination and correction. *J Struct Biol* 193: 1–12
- Zheng SQ, Palovcak E, Armache J-P, Verba KA, Cheng Y, Agard DA (2017) MotionCor2: anisotropic correction of beam-induced motion for improved cryo-electron microscopy. *Nat Methods* 14: 331–332

- Zivanov J, Nakane T, Scheres SHW (2019) A Bayesian approach to beam-induced motion correction in cryo-EM single-particle analysis. *IUCrj* 6: 5–17
- Zoued A, Brunet YR, Durand E, Aschtgen MS, Logger L, Douzi B, Journet L, Cambillau C, Cascales E (2014) Architecture and assembly of the Type VI secretion system. *Biochim Biophys Acta Mol Cell Res* 1843: 1664–1673
- Zoued A, Durand E, Brunet YR, Spinelli S, Douzi B, Guzzo M, Flaugnatti N, Legrand P, Journet L, Fronzes R et al (2016) Priming and polymerization of a bacterial contractile tail structure. *Nature* 531: 59–63